



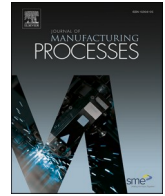
Influence of part geometry on spatter formation in laser powder bed fusion of Inconel 718 alloy revealed by optical tomography

Downloaded from: <https://research.chalmers.se>, 2024-04-26 08:01 UTC

Citation for the original published paper (version of record):

Chen, Z., Raza, A., Hryha, E. (2022). Influence of part geometry on spatter formation in laser powder bed fusion of Inconel 718 alloy revealed by optical tomography. *Journal of Manufacturing Processes*, 81: 680-695.
<http://dx.doi.org/10.1016/j.jmapro.2022.07.031>

N.B. When citing this work, cite the original published paper.



Influence of part geometry on spatter formation in laser powder bed fusion of Inconel 718 alloy revealed by optical tomography

Zhuoer Chen^{*}, Ahmad Raza, Eduard Hryha

Department of Industrial and Materials Science, Chalmers University of Technology, SE-412 96 Gothenburg, Sweden

ARTICLE INFO

Keywords:

Powder degradation
Reused powder in AM
Optical tomography
Process monitoring
Inconel 718

ABSTRACT

The metal powder used during the Laser Powder Bed Fusion (L-PBF) process is usually cycled for reuse in subsequent build jobs for cost-effectiveness and sustainability. Qualification guidelines are being established based on testing results of powder properties in terms of flowability, chemistry and rheological behaviors, etc. for making decisions on whether a batch of reused powder is suitable for producing parts that meet certain requirements. The current paper aims to develop experimental strategies for tracking powder history using novel design of specimens and on-line monitoring. Powder-capturing containers designed with internal lattice structures of varied beam lengths and diameters were manufactured by the L-PBF process using an Inconel 718 powder to investigate the influence of part geometry on the degradation of reused powder. The L-PBF experiment was monitored by a commercial Optical Tomography (OT) system which records the thermal emissions from the build area. Data were extracted from the OT images to evaluate the emissions of spatter particles introduced to the powder bed, which is influenced by the local layer profiles of the lattices and the overall geometries of the container. The collected powder samples were tested by combustion analysis for oxygen content and characterized by Scanning Electron Microscopy (SEM). Surface chemistry analyses of the powders were performed by X-ray Photoelectron Spectroscopy (XPS). Depending on the lattice structure geometry, the oxygen uptake in the powder collected from the containers was increasing by 10 ppm in case of empty container and up to as high as 118 ppm in case of container with larger areas of overhangs and higher surface-to-volume ratio. XPS results revealed the presences of Al-rich and Cr-rich oxides on the surface of powder samples collected from the container filled with lattices of high surface-to-volume ratio and the container filled with lattices of large overhangs, which agrees with the analyses of OT data.

1. Introduction

Laser Powder Bed Fusion (L-PBF) is one of the key metal additive manufacturing (AM) technologies that can produce functional components from a variety of materials with complex, customizable geometry and sufficient mechanical properties [1]. The L-PBF process uses a focused laser beam to melt thin layers of metal powders according to cross-sectional profiles of 3D design models to construct components in a layer-by-layer fashion. The powder not used for building the components is usually cycled, sieved, and used for subsequent building processes. However, laser interactions with the powder during the building process, as well as the storage and handling of powder under various environmental conditions, can introduce changes to the powder properties. Monitoring of powder history and its relevant evolution in characteristics through process cycles is therefore important for

producing L-PBF components with consistent properties [2].

The variation in the quality metrics of the metal powder feedstock through reuse cycles in L-PBF and Electron Beam Melting (EBM) processes has been the focus of numerous studies. It is reported in literature that the particle size distributions of powders shift due to the inclusion of spatter particles and satellites although the powders are sieved before reuse [3–5], which is known to affect the packing fraction and flowability of the powder [6,7]. The chemical degradation of powder is associated with two mechanisms, namely surface oxidation by the heating of powder bed, and progressive inclusion of spatter particles.

Firstly, in a commercial L-PBF system, the oxygen level is typically controlled at a level lower than 1000 ppm, which is not sufficiently low to prevent surface oxidation [8,9]. Based on simulations, in L-PBF process the powder in close proximity of the part is heated to elevated temperatures due to the heat conduction from the printed part [10].

^{*} Corresponding author.

E-mail address: zhuoer.chen@chalmers.se (Z. Chen).

<https://doi.org/10.1016/j.jmapro.2022.07.031>

Received 17 February 2022; Received in revised form 20 June 2022; Accepted 12 July 2022

Available online 20 July 2022

1526-6125/© 2022 The Authors. Published by Elsevier Ltd on behalf of The Society of Manufacturing Engineers. This is an open access article under the CC BY license (<http://creativecommons.org/licenses/by/4.0/>).

Alloying elements with high affinity to oxygen such as Al, Cr and Ti may diffuse to powder surface to form oxides at elevated temperatures with the presence of residual oxygen [8,11]. In the L-PBF processing of IN718 powder, thermodynamically stable Al-rich and Cr-rich oxides are favored to nucleate and grow on surface over thermodynamically less stable oxides such as Ni-oxide and hydroxide [8].

Secondly, during the laser-powder interactions, melt droplets are ejected from the melt pool resulting from complex fluid dynamics involving Marangoni flow and recoil pressure exerted by the metal vapor plume [12,13]. It is suspected that the oxidation of the ejected melt droplets takes place during their flight and solidification [14]. In addition, the powder surrounding the melt tracks can be directly ejected [15] or entrained by the metal vapor jet, inducing denudation of powder surrounding the melt pool [16–18]. A certain fraction of the entrained powder can move into the laser path to be irradiated by the laser, thus developing oxidized surface layer as the in-flight particles are subject to high temperature and residual oxygen [5,8]. Formation of Al-rich and Cr-rich oxide islands with high oxygen contents and large thicknesses on the surface of the spatter particles and entrained powder particles were observed in L-PBF processing of IN718, suggesting significant uptake of oxygen from the build chamber and the processed part [5,8].

As suggested by several studies on powder reusability, only recording the number of cycles the powder has experienced is not sufficient for the qualification of the reused powder. Goji et al. [19] suggested that the area of laser exposure should be recorded based on the observation that the powder in between laser-irradiated parts possess a larger fraction of spatter compared to the rest of the feedstock. Pauzon et al. [8] reported that the high surface-to-volume ratio of the lattice structures accelerates the generation of spatter, suggesting the geometry of the parts to be considered to evaluate and predict the powder usage of a certain build. Moghimian et al. [20] proposed to record the duration of each build, the build volume, the geometry and the powder bed volume for powder reusability study. The authors also emphasized the importance of blending powder sample before evaluation of degradation, since the degradation is not homogenous across the entire build area [20]. Furthermore, the gas flow in a L-PBF machine performs the functions of directing the process by-products towards the outlet, extracting heat from the laser-irradiated area, and providing inert gas atmosphere for prevention of chemical reaction between the reactive gas and processed material [21–23]. Different L-PBF machines employ different gas flow speed [24], inlet and outlet design [25,26], which results in different flow establishment over the build area [26,27] and affects the degradation of powder by modulating the laser-powder interactions and removal of process by-products [21].

Given the convoluted effects of part geometry, exposure area and gas flow, it is desirable to monitor the laser-powder interactions in real time, particularly the ejections of hot particles (spatter and entrained particles) into the powder bed, for evaluation of powder degradation. The current work demonstrates the use of long exposure images recorded by Optical Tomography (OT) system for evaluating the effects of part geometry on powder degradation. Through detailed analysis of the OT images and characterization of the powder samples, it is possible to link the signals recorded by OT to the degradation of powder.

2. Experimental methods

2.1. L-PBF experiment

The powder used by this study was virgin Inconel 718 (IN718) gas atomized powder supplied by Höganäs Germany GmbH. The nominal chemical composition was measured by the powder manufacturer using inert gas fusion method and is shown in Table 1. The L-PBF experiment was conducted using an EOS M290 machine applying default processing parameters (IN718 PerformanceM291 1.02) with a layer thickness of 40 μm . The build chamber was flooded with argon gas during the building process to maintain an oxygen level under 1000 ppm. The pre-heating temperature of the build plate was 80 $^{\circ}\text{C}$.

2.2. Specimen design

Container samples were designed to capture powder during the L-PBF process. The thickness of the side walls for all containers is 1.5 mm. The containers are self-supporting by design and are named after the length and diameter of the lattice beams, e.g., L7D3 (length = 7 mm and diameter = 3 mm). The lattice structures are all face centered tetragonal structure, as shown in Fig. 1a. Three of the containers, namely L7D3, L7D1 and L3D1, were filled with lattice structures and one was empty inside (Fig. 1b, c, d and e). The caps for the container were designed with a thin connection with the body of the container as pointed out by the arrow in Fig. 1b, so that the thin connection can be broken to take the powder samples out for analysis. The containers were placed close to the gas inlet on the build platform at the back side of the machine. The X, Y, and Z axes used throughout the current paper are defined in Fig. 1f with the origin located at the lower left corner of the build plate. The containers were built on top of fragmented support structure with a 2 mm thickness for the ease of removal after the build process is finished.

2.3. Optical tomography

The EOSTATE Exposure OT system is an on-line monitoring tool that takes measurements of the thermal radiation from the build area using an off-axis sCMOS (scientific complementary metal-oxide semiconductor) camera. Details regarding the hardware setup for the OT system is presented in detail elsewhere [28]. During the setup of the monitoring device, a build with simple geometry was conducted to acquire the necessary parameters to correct for the geometrical distortions due to the non-central positioning of the camera. The laser exposure of powder emits radiation from the melted area, which is collected by the sCMOS camera equipped with a bandpass filter @ $900 \pm 12.5 \text{ nm}$. The camera has a rolling shutter that refreshes every 0.1 s, which does not introduce deadtime to the long exposure image. Thus, each layer of the laser exposure is recorded by the OT system as a long exposure image containing the thermal radiation from the processed area represented by the brightness of pixels, i.e., grey value (GV). The GVs recorded by the OT system are integrated over the period of processing of the respective layers, and therefore are also referred to as integral grey values (Int GVs). The OT camera has a stationary field of view covering the entire build area of 250 mm \times 250 mm with each pixel covering an area of 0.125 mm \times 0.125 mm, thus yielding 2000 \times 2000 pixels for each layer

Table 1
Chemical composition of IN718 powder used in this work.

Elements	Ni	Cr	Nb	Mo	Ti	Al	C	B
wt%	53.8	19.0	5.43	2.0	1.0	0.5	0.04	<0.002

Elements	Co	Cu	Mn	N	P	S	Si	Fe
wt%	0.0	<0.01	<0.01	0.008	<0.005	0.002	<0.1	Bal.

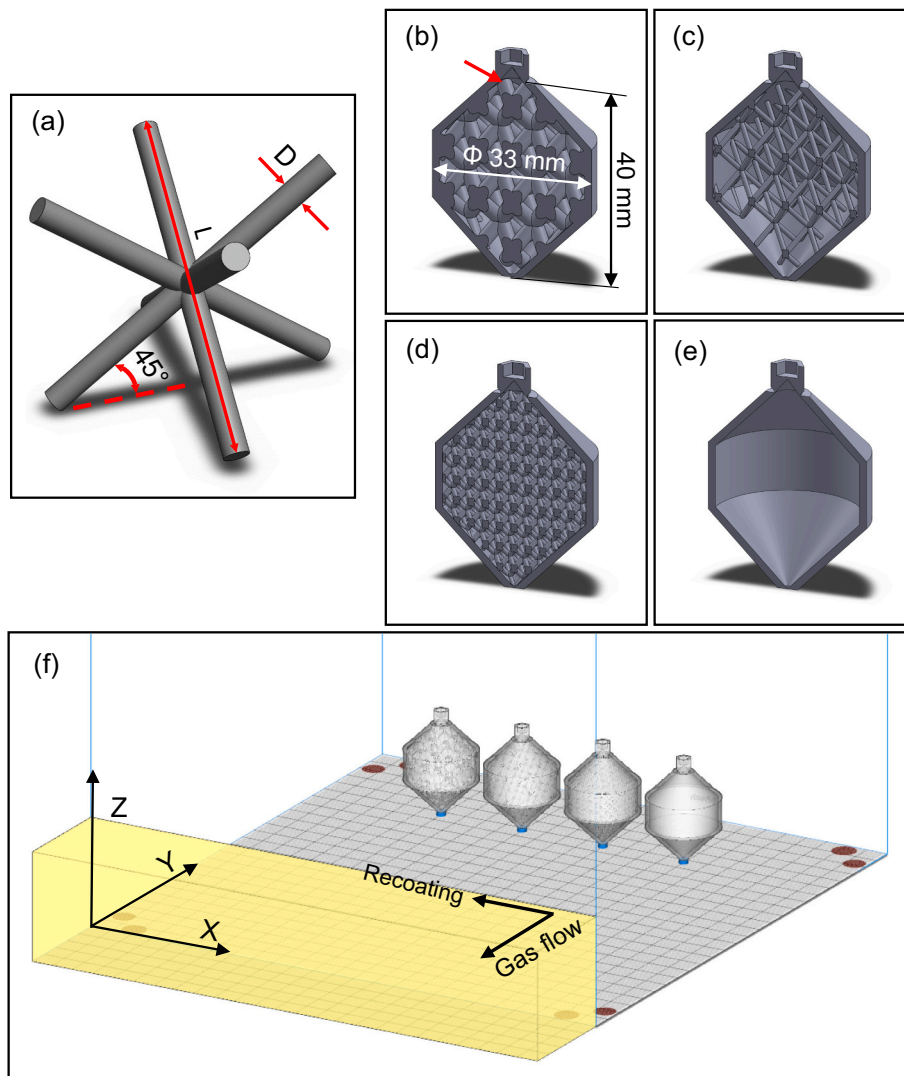


Fig. 1. Specimen designed to encapsulate powder during L-PBF process: (a) unit cell design for lattice structure features a face centered tetragonal structure with the beams at 45° to the horizontal plane; cross-sectional view of four variants of container design (b) L7D3, (c) L7D1, (d) L3D1, (e) empty. The red arrow in (b) points to the break point to collect powder samples. (f) Placement of the four specimens in an EOS M290 build chamber, the position of the gas outlet where a powder sample was taken is indicated by the yellow box. The coordinate system is indicated with its origin at the lower left corner of the build plate. (For interpretation of the references to color in this figure legend, the reader is referred to the web version of this article.)

of laser exposure.

For analysis of the OT results, 16-bit images were imported to MATLAB software to read the GVs from each pixel along with the coordinates of the pixels. In OT images, pixels belonging to the laser scanned area designated by the STL files of the part model show certain GVs representing the melt pool intensities. In addition, pixels that are outside of the laser scan path can also contain GVs, which can be used to evaluate the emissions from incandescent spatter particles generated by the L-PBF process. These two types of pixels are referred to as laser-irradiated region and spatter region for the rest of the manuscript.

A meshed geometry of the part is created using a voxel size with dimensions of a pixel size in x-y plane and one layer thickness in the build direction. The voxelization was done using a MATLAB code developed by Aitkenhead [29], the code uses a ray intersection method similar to the method in [30]. A logical array was created using the meshed geometry of the part as a mask which was then used to separate the pixels from the laser-irradiated region from the rest of the image.

2.4. Particle size distribution measurements

Powder particle size distributions were measured for the powder samples collected in virgin state and from the four container samples using a Mastersizer 3000 equipment from Malvern (Malvern, UK). The measurements were repeated five times for each powder sample for

statistical significance.

2.5. Surface characterization and oxygen content measurement

The bulk oxygen contents of the powder samples were measured by combustion analysis (inert gas fusion) using a LECO ON836. The collected samples were also analyzed by means of high-resolution scanning electron microscopy (HR-SEM) for surface morphology and microstructure, and X-ray photoelectron spectroscopy for surface chemical state. The HR-SEM used was a LEO Gemini 1550.

The effects of the L-PBF processing on surface chemistry, oxide composition, oxide layer thickness, and penetration depth were investigated using X-ray Photoelectron Spectroscopy (XPS) using PHI 5500 (ULVAC-PHI). The PHI 5500 was equipped with a monochromator Al K α source (1486.6 eV). To avoid the damage to the powder surface during the sample preparation, the powder particles were mounted on Indium template. The analysis area was $300\ \mu\text{m} \times 300\ \mu\text{m}$ for each sample, which enables a large population of powder particles (50–100, depending on the particle size) to be examined. The pass energies used were 224 eV and 26 eV for survey scan and narrow scan respectively. For depth profile analysis, Ar $^{+}$ ion gun was used where the etch depth is calibrated against a standard Ta $_2$ O $_5$ sample, and the depth is given in Ta $_2$ O $_5$ units. The data obtained from XPS was analyzed using PHI Multipack software.

3. Results

3.1. OT images

The influence of layer profiles on the amount of spatter particles

generated during the laser processing of powder can be inferred from the observations of OT images. In Fig. 2, the color scales of the OT images are adjusted to make the spattering events more obvious to the reader (Fig. 2). For illustration, at $Z = 18$ mm in Fig. 2, the spatter particles with longer trajectories are indicated by orange arrows, and the ones with

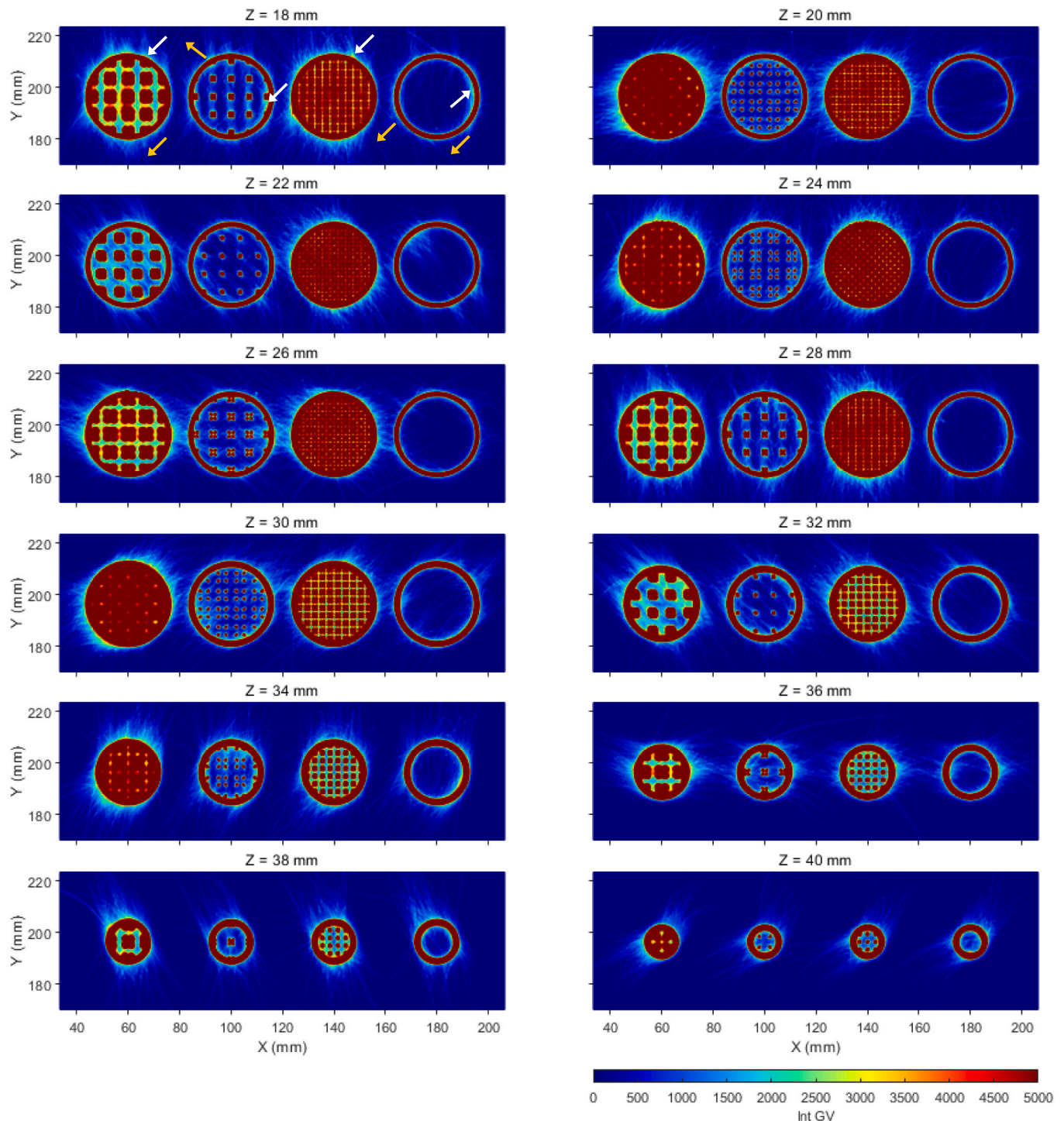


Fig. 2. OT images at different build heights. From left to right in each image the specimens are the L7D3, L7D1, L3D1 and empty containers. The maximum level of color scale for GV is adjusted to a relatively low value of 5000 to make the trajectories of spatter particles better visible. The areas laser-irradiated by the laser are predominantly red in color due to the adjusted color scale. At $Z = 18$ mm, the white arrows point towards spatter particles with short trajectories at the vicinity of part boundaries, the orange arrows point towards spatter particles with longer trajectories. The spattering appears in all layers presented and is highlighted at $Z = 18$ mm as an example. The raw OT images, images for irradiated regions, and images for spatter regions at these corresponding build heights are available in supplementary Fig. S2, S3, and S4. (For interpretation of the references to color in this figure legend, the reader is referred to the web version of this article.)

shorter trajectories are indicated by white arrows. The incandescent spatter particles with longer trajectories generally show lower GVs compared to those with shorter trajectories. As the spatter particles depart from the melt pool the temperature of these particles drops rapidly, emitting weaker light signals to the OT camera. The majority of the spatter particles, particularly the ones with longer trajectories, travel along the direction of laser scan [18], whereas during the flight their trajectories are influenced by the directional gas flow to some extent. Consequently, the spatter is found to travel along various directions in the OT images shown in Fig. 2 due to the rotation of laser scan orientation between layers.

As one compares the GVs surrounding the laser scanned areas of different containers, it is apparent that the L7D3 and the L3D1 containers possess stronger signals in the spatter region, the origin of such stronger signals should be clarified. Unlike the L7D1 and the empty containers, it is not possible to see individual trajectories of spatter at the interiors of the L7D3 and the L3D1 containers. This is likely a result of many overlapped trajectories of spatter particles, adding up to greater GVs captured by the long exposure OT camera. Additionally, for a given container, the layer profiles on the XY planes change along the build direction (Z), which also affects the GVs at the cavities in the containers not scanned by the laser. For instance, in the L7D3 container, the gaps between lattices show much higher GVs at Z heights of 20 mm, 24 mm, 30 mm and 34 mm as compared to the rest.

3.2. Influence of part geometry on OT data

Each OT image can be divided into three regions, namely the laser-irradiated region, the spatter region, and the zero GV region that is not affected by the laser irradiation or spattering. The laser-irradiated region is separated from the rest using the methodology described in Section 2.3. A further division is made between the spatter region and the zero GV region depending on the GV of the pixel is zero or not. The coordinates of the pixels are known by their locations in an OT image and the layer height at which the OT image was taken; thus, the OT images can be used to reconstruct 3D volumetric data for each container sample. It should be emphasized that the analysis of the spatter regions in the OT images is restricted to the bounding boxes of the containers to avoid interferences between neighboring containers as the containers were placed relatively close to one another (Fig. 2).

Due to the differences in lattice structures, the containers vary significantly in the quantities listed in Table 2. The larger the volume of solid is, the smaller the cavity inside the container becomes. The number of pixels detected as spatter region is not a direct indication of spatter amount due to the overlapping of spatter trajectories, which make it necessary to analyze the GVs in these pixels for implications for powder degradation. Fig. 3 shows the distributions of GVs in OT images collected from the four containers. The histograms for the laser-irradiated and the spatter regions in the OT images show only small overlaps around 10^4 GV. The L7D3 and L3D1 (Fig. 3a and c) containers show generally higher GVs in the spatter region (blue histogram) compared to the L7D1 and empty containers (Fig. 3b and d). Meanwhile, the L7D3 container shows higher GVs in the laser-irradiated region (red histogram) compared to the other three containers.

To elucidate the influence of lattice geometry on spatter generation

in the container samples, various quantities are calculated for each layer of the process according to Eq. (1)–(6) and compared.

$$f_l = N_l/N \quad (1)$$

$$f_s = N_s/N \quad (2)$$

$$S_l = \sum_{i=1}^{N_l} GV_{li} \quad (3)$$

$$S_s = \sum_{i=1}^{N_s} GV_{si} \quad (4)$$

$$\mu_l = S_l/N_l \quad (5)$$

$$\mu_s = S_s/N_s \quad (6)$$

The terms used have the following significance:

- f_l, f_s – area fraction of the laser-irradiated region and spatter region in an OT image,
- N_l, N_s – pixel counts in the laser-irradiated and spatter regions,
- N – total number of pixels evaluated in an OT image,
- GV_l, GV_s – grey value of a pixel recognized as the laser-irradiated and spatter regions,
- S_l, S_s – sum of GVs in an OT image for the laser-irradiated and spatter regions,
- μ_l, μ_s – mean of GVs in an OT image for the laser-irradiated and spatter regions.

The area fractions of the laser-irradiated regions depend solely on the layer profiles of each container. For the three containers filled with lattices, the area fractions of the laser-irradiated regions reach local maximum where the lattice beams diverge farthest away from the vertices underneath and drop to local minimum as the lattice beams converge at vertexes. The area fractions of the spatter regions, however, depend on both the layer profiles and the amount of spatter particles generated during the L-PBF process. A larger area of the laser-irradiated region in a layer leads to less space available for the spatter to be detected. Meanwhile, the layer profiles of the containers also influence the amount of spatter generated, resulting in a different coverage of the area by spatter trajectories. The sums of GVs per layer for the laser-irradiated region and the spatter region can be associated with the thermal radiation from the laser-irradiated region and the amount of spatter particles introduced to the surrounding powder bed, respectively. The means of GVs in each layer for the laser-irradiated region and the spatter region indicate the average emissions from the melt pool and incandescent spatter, respectively.

3.2.1. Local variations within the container samples

The quantities calculated in Eqs. (1)–(6) are plotted for the L7D3 container in Fig. 4 to show the variation along the build direction as the layer profile changes for each container filled with lattices. The area fractions, the sums and means of GVs of both the laser-irradiated and the spatter regions change in a periodical manner with a wavelength equivalent to the projected heights of lattice beams on the Z axis, $\lambda = L$

Table 2

Quantities describing the geometry of the containers, namely the volume of solid, surface area, and volume of cavity, and pixel counts in laser-irradiated region, spatter region and region of no signal (zero GV) calculated from OT images from all layers for individual containers.

Containers	Volume of solid ($\times 10^4 \text{ mm}^3$)	Surface area ($\times 10^4 \text{ mm}^2$)	Volume of cavity ($\times 10^4 \text{ mm}^3$)	Pixel count in laser-irradiated region ($\times 10^7$)	Pixel count in spatter region ($\times 10^7$)	Pixel count in zero GV region ($\times 10^7$)
L7D3	1.35	1.33	0.76	2.18	3.52	1.32
L7D1	0.64	1.13	1.47	1.04	4.49	1.49
L3D1	1.09	2.67	1.02	1.76	3.94	1.32
Empty	0.52	0.69	1.59	0.84	4.01	2.17

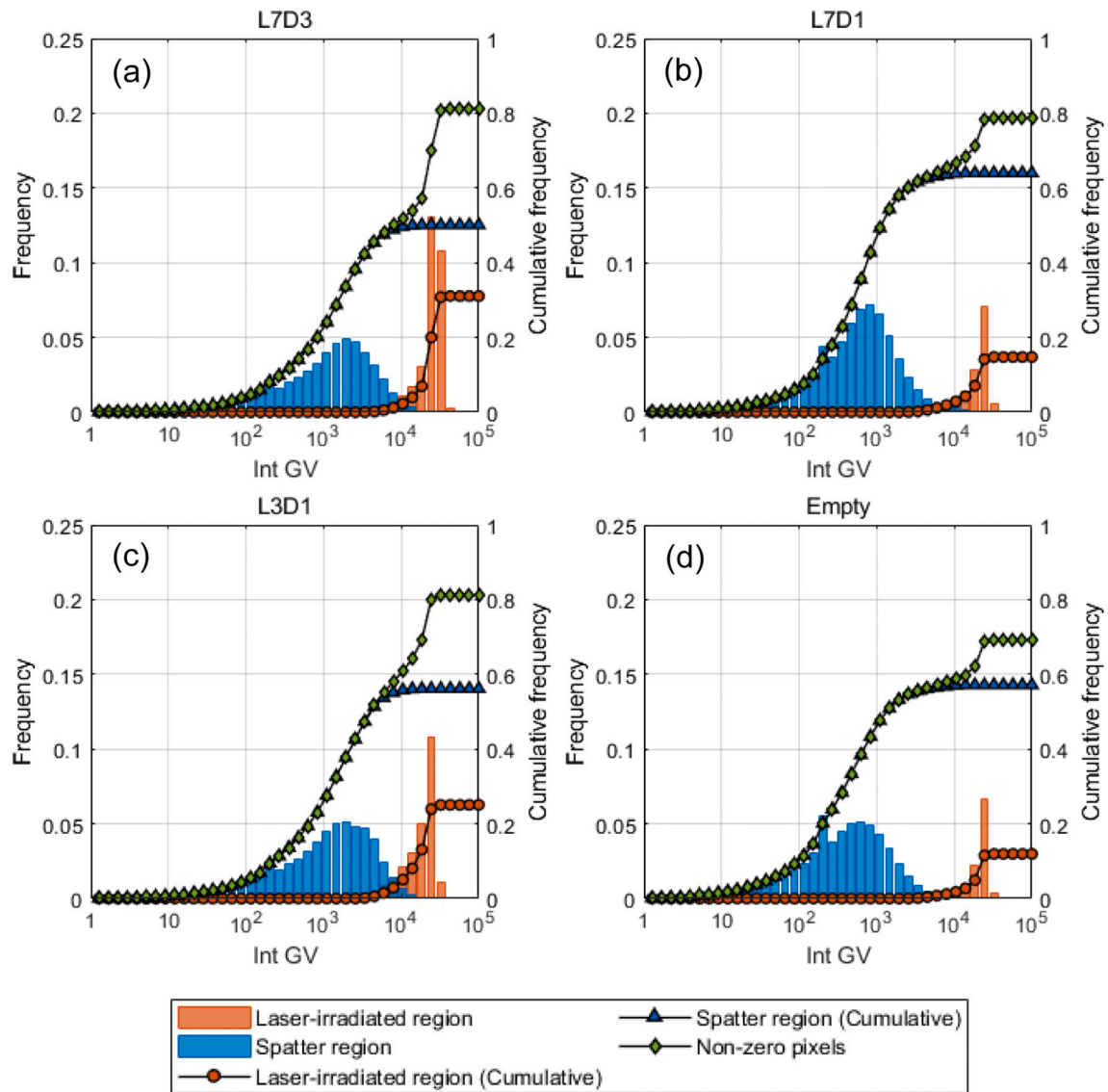


Fig. 3. Histograms of GV values in the OT images of all layers identified as the laser-irradiated regions and the spatter regions for the (a) L7D3, (b) L7D1 (c) L3D1 and (d) empty containers. The frequency values are normalized by the total count of pixels in the bounding boxes of the container samples. On the right axes, the cumulative frequencies for both regions are plotted. The cumulative frequency of non-zero pixels combines both regions. The cumulative frequency plots of non-zero pixels do not reach unity since there are zero GV pixels present in the evaluated volumes.

$\times \sin 45^\circ$, where L is the length of the lattice beam. λ is approximately 4.95 mm for the L7D3 and the L7D1 containers and 2.12 mm for the L3D1 container.

As shown in Fig. 4 for the L7D3 container, in the laser-irradiated region, it is natural that the sums of GV values would increase with increasing area fractions of the laser-irradiated region. However, the means of GV values in the laser-irradiated region also increase, which is obvious as one compares the colormaps in Fig. 4a second column. This implies higher melt pool intensity in the laser-irradiated region as the lattice beams diverge from the vertexes to form large overhang areas. Meanwhile, the sums and means of GV values in the spatter region are maximized at layers where the area fraction of the spatter region is locally minimal (e.g., $Z = 24.88$ mm in Fig. 4b). This indicates that as the total area of laser exposure increases in the L7D3 container, the spatter trajectories appear in the powder bed surrounding the part with higher frequency. Similar presentations of local variations in the L7D1 container and the L3D1 container are available in the supplementary material.

3.2.2. Comparison among the container samples

Fig. 5 compares the calculated quantities in Eq. (1)–(6) for the four containers across the full sample height excluding the bottom support structure and the cap on the top. The lattice structures in the L7D3 and the L3D1 containers occupy significant area fractions in the OT images (Fig. 5a), which limits the area fractions of spatter region (Fig. 5b). The L7D3 container has the lowest overall area fraction of spatter region due to its large volume of solid (area of laser exposure in 2D). The L7D1 container shows the highest area fraction of spatter region (Fig. 5b) since there are ample space between the lattice beams and the lattices inside the container act as origins of spatter. The empty container has the most space for spatter emission to be recorded, but since there is no laser exposure inside the container, the area fraction of spatter region in the empty container is not the most.

The means of GV values in the laser-irradiated region, as a measure of average laser energy input to the material per unit area, are much higher in the L7D3 container (Fig. 5e), which suggests overheating in the L7D3 container. The higher sums of GV values in the laser-irradiated region of the L3D1 container as compared to the L7D1 container and the empty

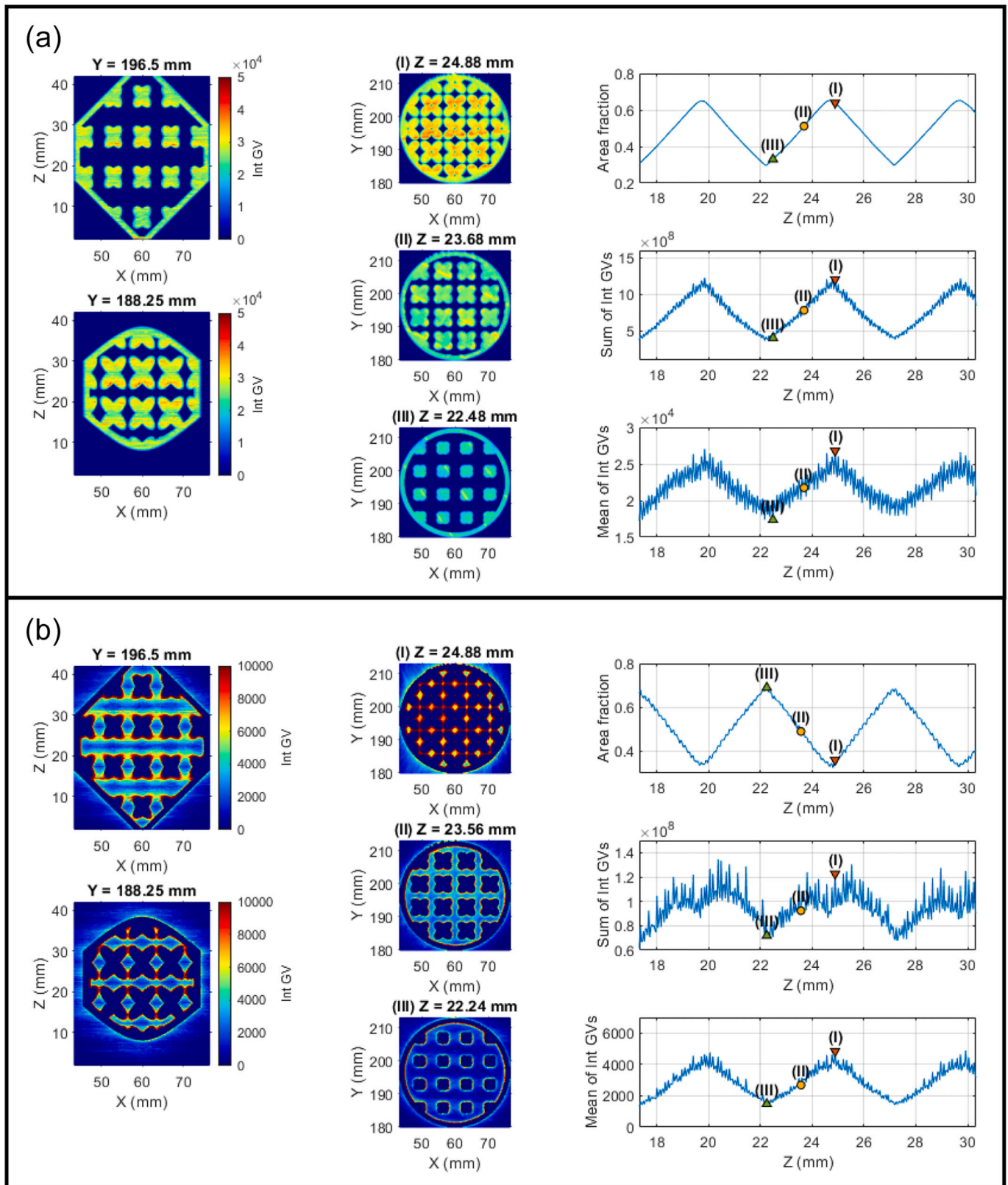


Fig. 4. Data extracted from the OT images of the L7D3 container for (a) the laser-irradiated region and (b) the spatter region. In each part, the first column shows two XZ cross-sections of reconstructed OT data at Y = 196.5 mm (mid-plane) and 188.25 mm (half radius away from the mid-plane). The second column shows XY cross-sections at Z coordinates where (I) local maximum and (III) minimum means of Int GV/s are found in the respective region of OT data and (II) is the mid-point on Z axis between (I) and (III). In the third column the area fraction, sums of Int GV/s, and mean of Int GV/s are presented for (a) the laser-irradiated region and (b) spatter region with the data at the three chosen Z heights indicated by markers and texts.

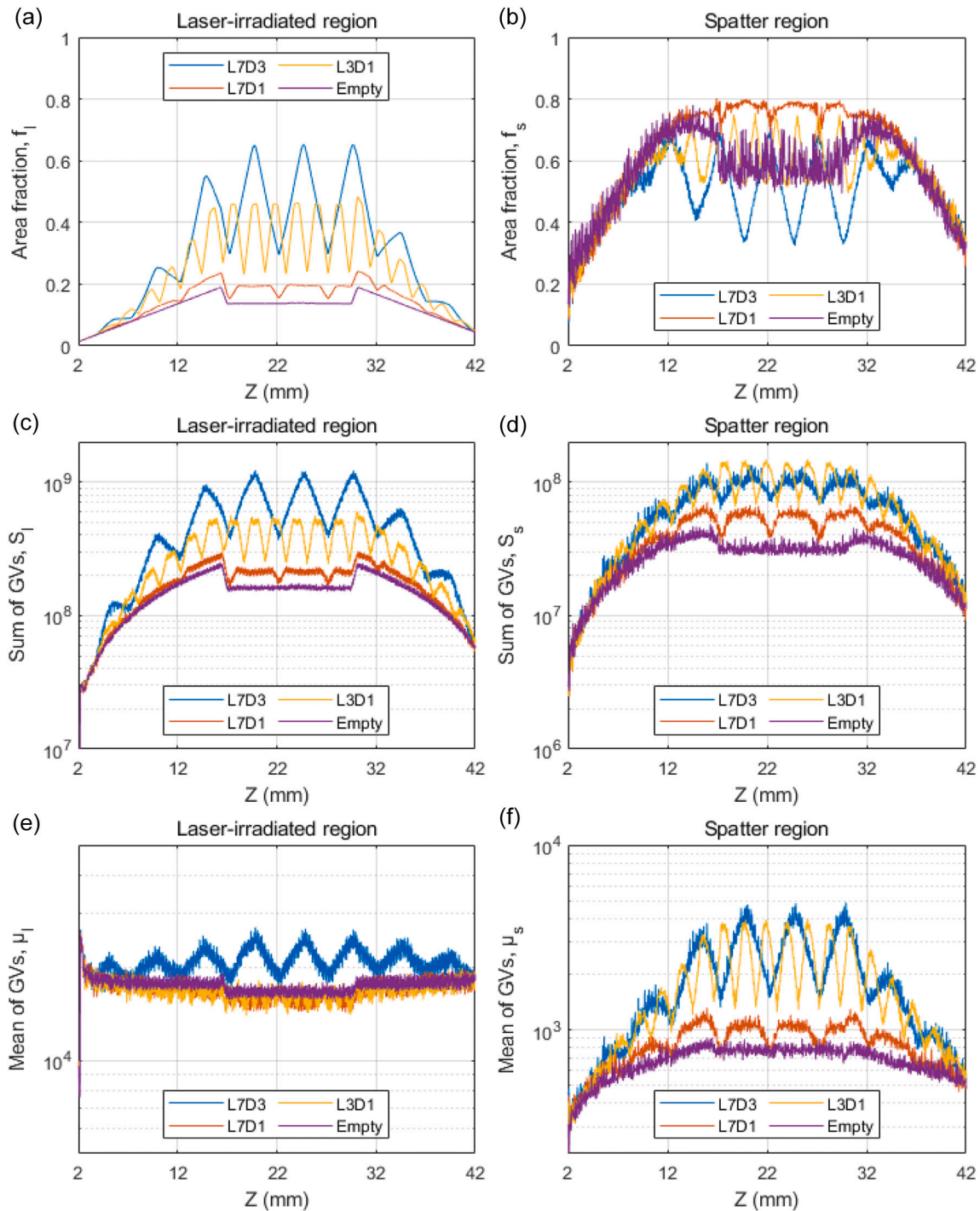


Fig. 5. Comparisons of (a), (b) area fractions, (b), (c) sum of Int GVs per layer, (e), (f) mean of GVs for the laser-irradiated region and the spatter region in the OT images at Z heights ranging from 2 mm to 42 mm where the powder samples are captured for the four different containers.

container are attributed to the higher area fractions of the laser-irradiated region. By contrast, the higher sums of GVs in the laser-irradiated region of the L7D3 container are caused by the higher means of GVs and larger area fractions in the laser-irradiated region.

Despite the significantly lower sums and means of GVs found in the laser-irradiated region of the L3D1 container as compared to the L7D3 container, the sums and means of GVs in the spatter regions of the two containers are of similar magnitudes. This implies that a large amount of spatter can be formed in two different ways: (1) laser exposure of large areas that experience high laser energy input, like the case of the L7D3 container, (2) laser exposure of parts with thin features that are closely

packed where the laser energy input is not as high, like the case of the L3D1 container.

3.3. Particle size distribution

Fig. 6 shows the particle size distribution plots of the powder samples collected in virgin state, and from the four containers. The D10, D50 and D90 of the five powder samples are listed in Table 3. The virgin powder possesses a slightly coarser size distribution compared to the four container samples, while the four samples from the containers show similar size distributions. It has been reported before that the virgin

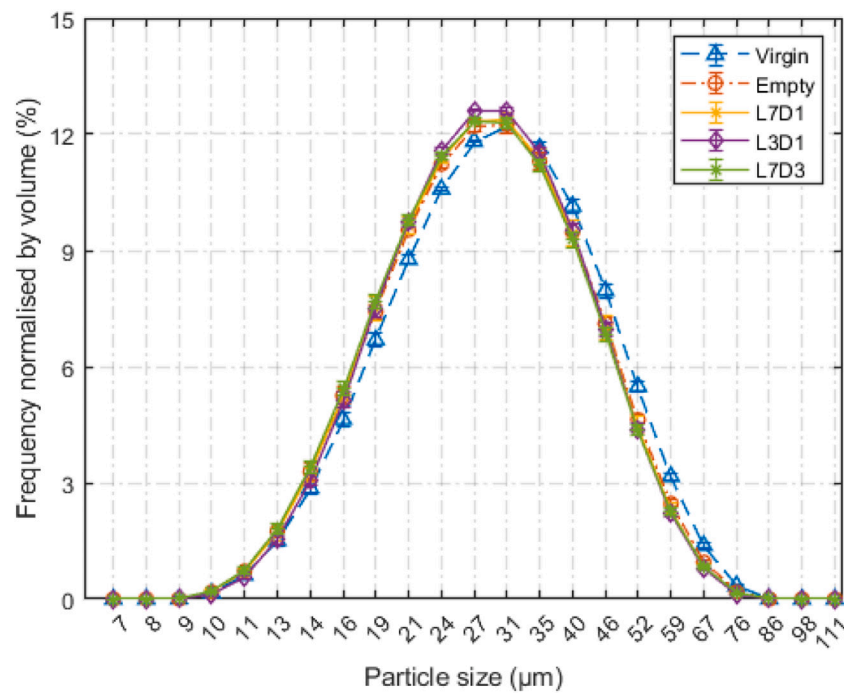


Fig. 6. Particle size distribution of the virgin powder and the four powder samples collected from the four container samples. The error bars area shown as one standard deviation derived from five repeated measurements. The bins are equally spaced on natural logarithmic scale, with a step size of 0.054, i.e., $\ln(S_{i+1}) - \ln(S_i) = 0.054$, where S_i is the position of the i th bin of particle size.

Table 3

D10, D50, and D90 for powder samples in virgin state and collected from the four containers.

Sample	D10 (μm)	D50 (μm)	D90 (μm)
Virgin	18.7	31.9	52.3
Empty	18.1	30.6	50.2
L7D1	18.2	30.4	49.7
L3D1	18.5	30.5	49.5
L7D3	18.0	30.2	49.5

powder can possess a coarser size distribution compared to used powder [3]. The only noticeable difference among the four containers is that the L3D1 powder shows slightly higher volume fraction in the size range of 27–31 μm. As is suggested by Whiting et al. [31], laser diffraction method incurs inaccuracies as it does not measure powder morphology and tends to overestimate the frequency of coarser particles. Methods such as Dynamic Image Analysis and SEM (static image analysis) are recommended in the future for more accurate characterization of powder size and morphology. It is also shown in [32] that the roughness of the part surface plays a vital role for the particle size distribution of powder spread on the part and in the vicinity of the part, such effects are not considered in the current paper and should be investigated for future works. Nevertheless, the spatter particles that are generated during the L-PBF process are not necessarily all large particles and cannot be removed from the used powder by sieving. This makes it necessary to examine chemical composition and surface oxide state to evaluate the powder degradation through L-PBF process cycles.

3.4. Oxygen content

Bulk oxygen contents measured through combustion analysis provide a rapid estimation of powder degradation during the L-PBF process. The oxygen content in the powder samples collected from the four containers, the virgin powder and the powder collected from gas outlet are compared in Fig. 7. The virgin powder contains 240 ppm oxygen,

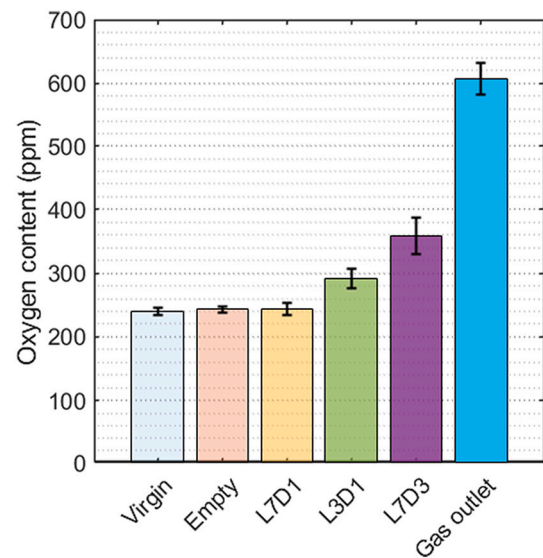


Fig. 7. Oxygen contents in the powder from the four cylinders, the virgin powder, and the outlet powder.

which is typical for such a powder. The powder collected from the gas outlet are the particles that are generated during the laser-powder interaction and are carried by the gas flow to reach the outlet. The outlet powder contains the highest content in oxygen (608 ppm), almost three times as much as the oxygen content in the virgin powder, similar to what is reported in the literature [8]. The samples collected from the four containers show oxygen levels between those of the virgin powder and the spatter powder collected at gas outlet, as they are essentially mixtures of virgin and powder oxidized during the L-PBF process. Among the four samples from the containers, powder from the L7D3 container contains the highest oxygen level at 358 ppm, followed by the samples from the L3D1 (292 ppm), L7D1 (243 ppm) and empty (243

ppm) containers. It is noteworthy that the oxygen contents in the powder samples collected from the empty and L7D1 containers are close to that of the virgin powder, indicating insignificant degradation.

3.5. Surface analysis of powder

Fig. 8 shows the overall appearances of the virgin powder, the powder samples collected from the containers and the gas outlet. The powder samples from the four containers show similar sizes and shapes compared to the virgin powder, while the powder particles at the gas outlet are significantly larger in size and show signs of severe surface oxidation. Fig. 9 shows an example of powder sample collected from L7D3 container where the two types of powder affected by the process are identified in addition to the unaffected powder particles (Fig. 9a). The powder unaffected by the process shows surface with no obvious sign of oxidation (Fig. 9b). The first type of powder affected by the process is surface oxidized powder (type I in Fig. 9a). These powder particles appear in spherical shape and possess many nano-scale oxide particulates on the surface (Fig. 9c). Oxidation in IN718 powder is

generally connected with oxidation of Al and Cr elements in the form of particulates instead of forming a uniform oxide layer [11]. This has been previously observed in EBM [33] and L-PBF reused powders [8]. In the empty container, such particles were not found but appeared in substantial amount in the L7D3 and L3D1 containers. The second type of particles affected by the L-PBF process (type II in Fig. 9a) shows higher extent of surface oxidation compared to the first type and appear brighter in SEM images. Islands of oxides were found on the surface of such particles (Fig. 9d). These particles are easily identified at low magnifications in Fig. 8c, d, and e as indicated by arrows, and are suspected to be spatter particles.

The XPS spectra for the powder samples under comparison (Fig. 10) show the elements present on the powder surface: carbon (C1s), oxygen (O1s), nickel (Ni2p), chromium (Cr2p), titanium (Ti2p), aluminum (Al2s), and indium (In3d). Indium peaks appear since indium substrate was used for mounting powder samples. Among all the samples, the Al2s and Al2p peaks appear with the strongest intensities in the outlet sample and the same peaks with lower intensities were observed in the L3D1 and the L7D3 samples. In the L7D1, empty and virgin powder samples,

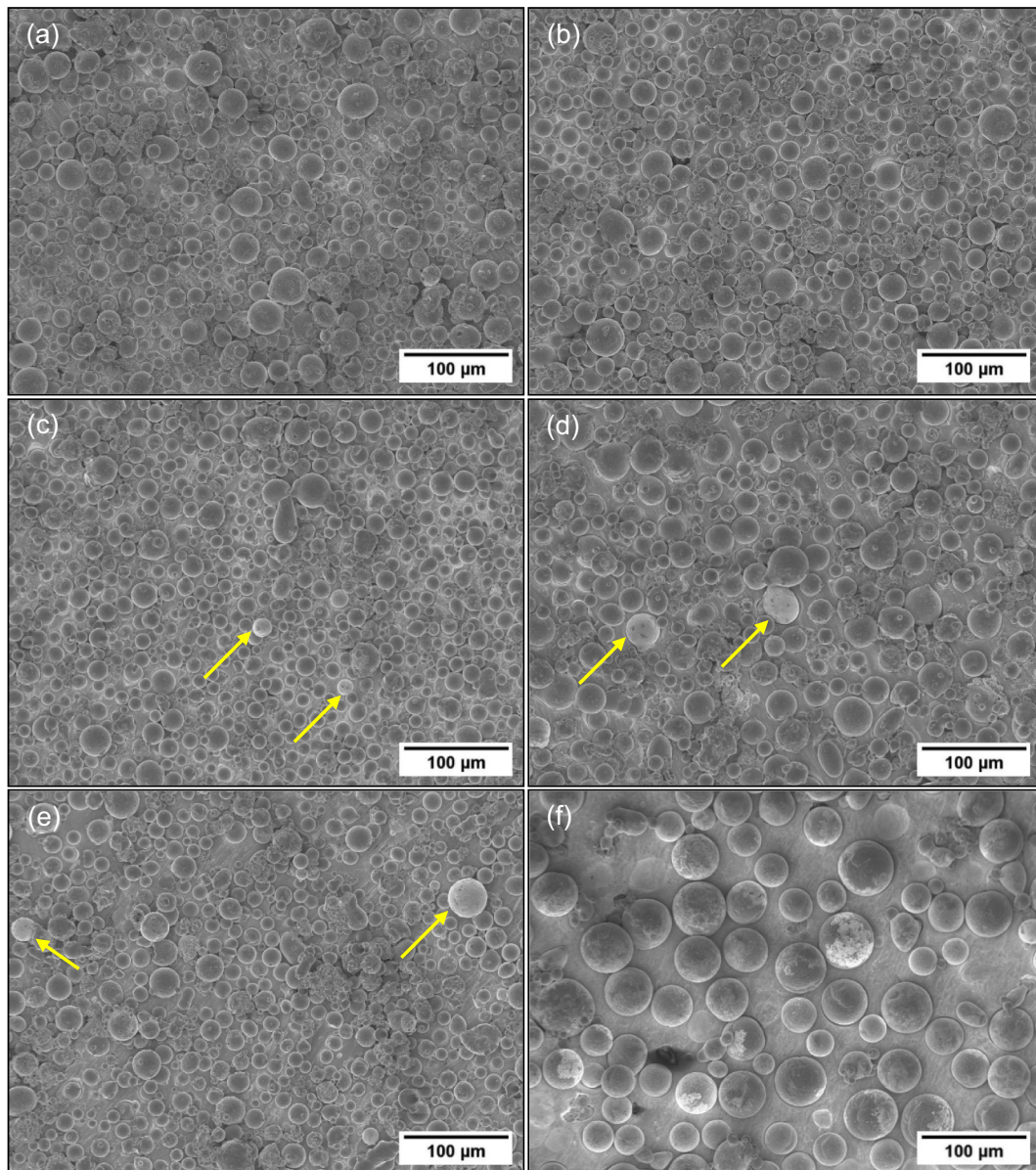


Fig. 8. SEM images of (a) virgin powder, powder collected from the (b) empty, (c) L7D1 (d) L7D3, (e) L3D1 containers and (f) powder collected from the gas outlet.

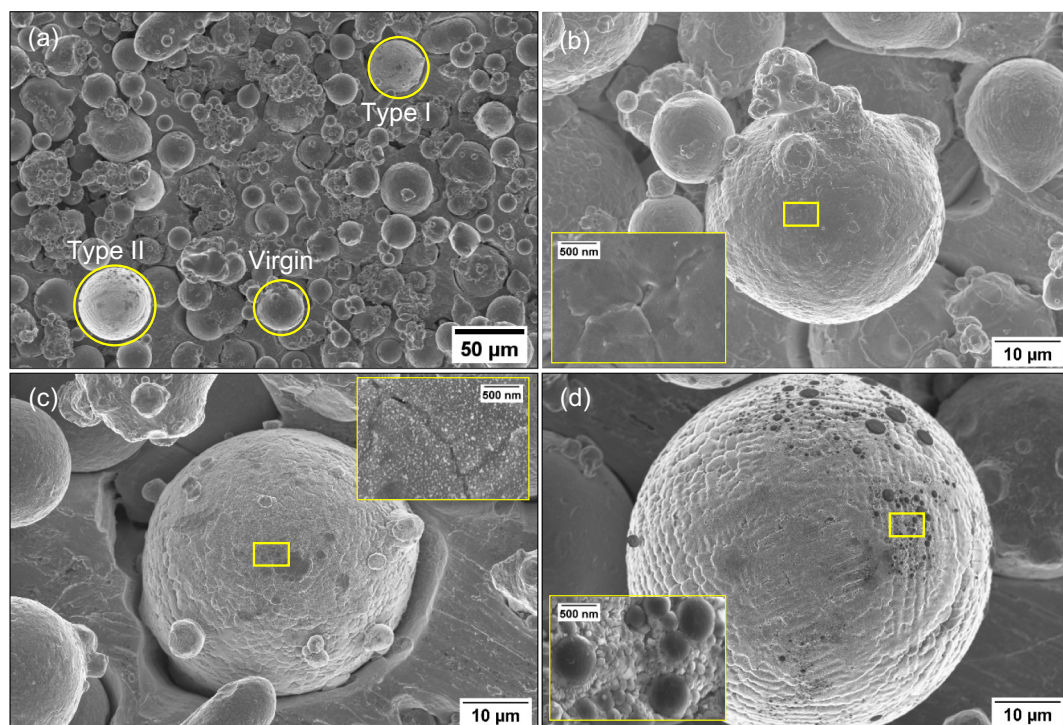


Fig. 9. SEM images of powder sample collected from L7D3 container. (a) overview image with different types of powder particles identified. (b) A particle unaffected by the L-PBF with non-oxidized surface. (c) A particle showing presence of nanoscale oxide particulates on surface, shown as type I powder in (a), (d) A particle with heavy surface oxidation, featuring oxide islands, shown as type II powder in (a).

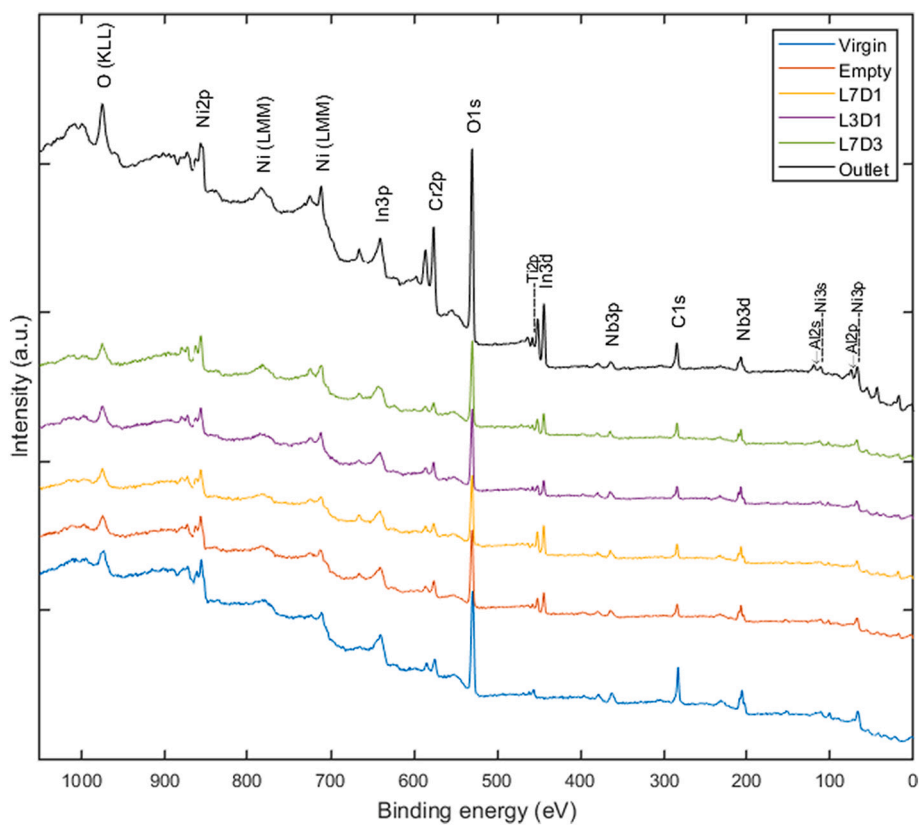


Fig. 10. XPS survey spectra of the virgin powder, the powder samples collected from four containers and the gas outlet.

no obvious Al2s or Al2p peak was found. Likewise, the Cr2p peaks appear the sharpest for the outlet powder and significantly weaker for the samples in the four containers and the virgin powder. The Ti2p peak only appear as a small peak in the outlet powder at ~ 459 eV, and not

distinguishable in other powder samples.

Narrow XPS spectra at higher resolution were used to analyze the chemical states of the selected elements. Depth profiling was used to estimate the oxide thickness for different powder samples. The depth

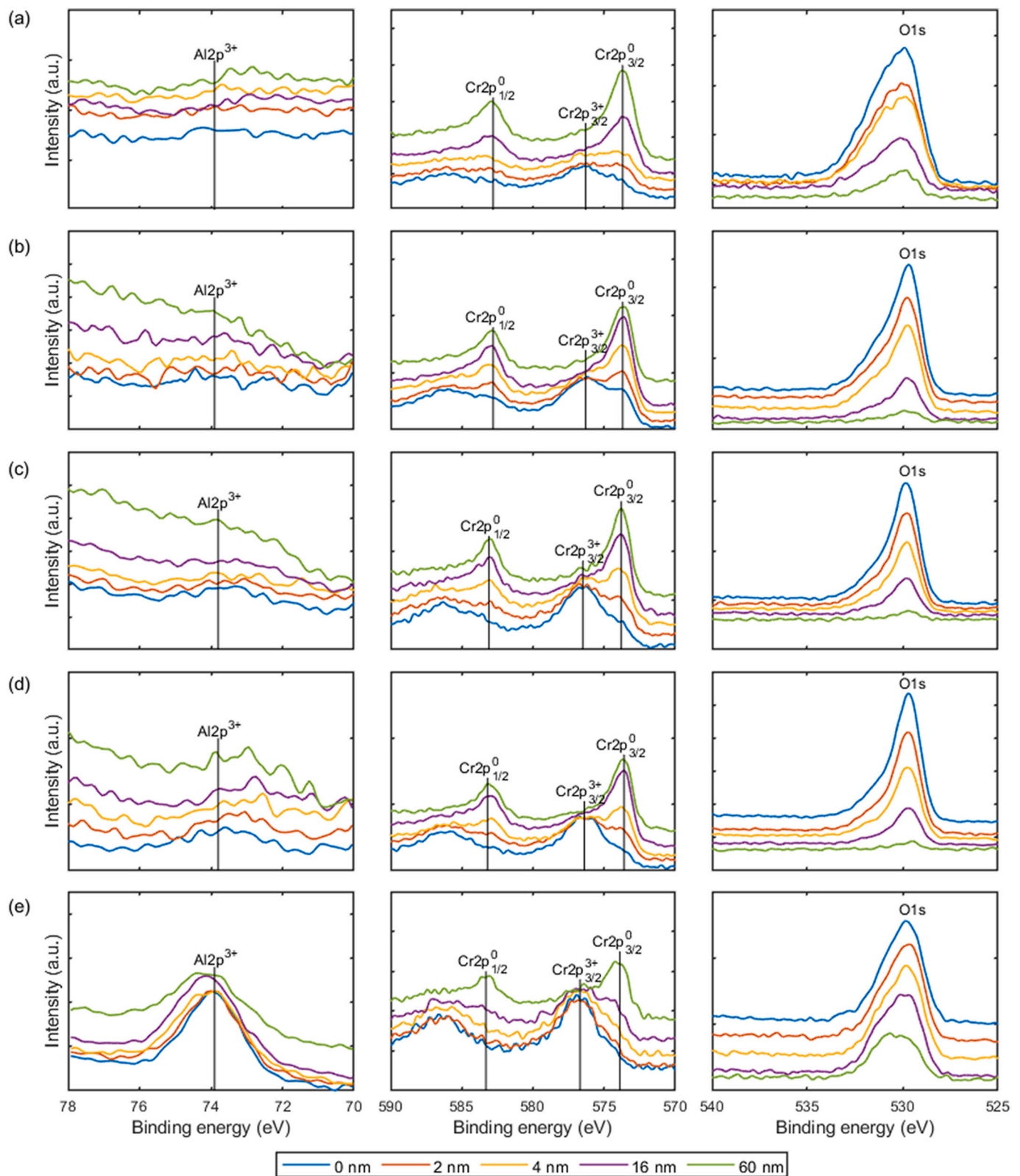


Fig. 11. Depth profiles of narrow XPS surveys showing Cr, Al, and O peaks for (a) the virgin powder, the powder samples collected from the (b) empty, (c) L7D3, (d) L3D1 containers and (e) the gas outlet.

profiles of Al2p, Cr2p, and O1s narrow spectra were acquired. In the Al2p spectra, there is no recognizable peak of Al2p³⁺ in the virgin powder and the powder collected from the empty container (Fig. 11a and b). In both the L7D3 and L3D1 containers, the powder samples show weak Al2p³⁺ peaks at initial depths from as-received surface (0 nm) to 4 nm (Fig. 11c and d). This indicates that a thin layer of Al-rich oxides is present on the powder surface. The outlet powder sample (Fig. 11e) shows strong Al2p³⁺ peaks across all etch depths, indicating presence of the Al-rich oxides on the surfaces of spatter particles with thickness larger than the final etch depth, i.e., 60 nm.

In the Cr2p spectra, a Cr2p_{3/2}³⁺ (Cr-oxide) peak appears at the as-received surface (0 nm) and is observed until 16 nm etch depth in the virgin powder and powder from the empty container, after which only metal peak of Cr is observed, highlighting that a thin layer of Cr-rich oxide is present on the powder surface, see Fig. 11a and b. The L7D3 and L3D1 powder samples seem to possess slightly thicker layer of Cr-rich oxide on powder surfaces as the Cr2p_{3/2}³⁺ peaks have higher intensity at etch depths of 4 nm and disappear completely at 16 nm depth (Fig. 11c and d). The outlet powder exhibits a much larger thickness of Cr-rich oxides like the case of Al-rich oxides as the Cr2p_{3/2}³⁺ peak still show considerable intensity at etch depth of 60 nm (Fig. 11e).

In the O1s spectra, no noticeable difference can be observed from narrow spectra for the virgin powder and the samples collected from the empty, L7D3, and L3D1 containers (Fig. 11a, b, c, and d), but a substantial peak broadening and presence of O1s peak at larger depth was observed for the outlet powder (Fig. 11e), connected to the larger content of Al-rich oxides.

4. Discussion

4.1. Use of OT images for tracking powder degradation

The relationship between the energy input during the L-PBF process as a result of varied processing parameters and the monitored characteristics of spatter were elucidated by several studies, which have implications for part qualification and process optimization [34,35]. Repossini et al. [34] and Taheri Andani et al. [35] performed in-situ monitoring of spattering with a high-speed camera placed outside the processing window. The grey-scale images collected were processed with image thresholding and segmentation to extract information about the spatter particles. Statistical descriptors of spatter such as convex area, number of spatter particles, pixel counts were found to be strongly affected by the laser energy input controlled by processing parameters [34,35]. Furthermore, a novel monitoring setup using two high-speed stereovision cameras with accompanying vision algorithms was developed by Barrett et al. [36] to track spatter trajectory in 3D space, velocity and lifetime – the length of time when spatter remains hot enough to emit detectable light to the cameras.

Since the purpose of the current study is to track the powder degradation rather than to evaluate process stability, the approach chosen for monitoring the spattering during L-PBF is different from the existing literature. Firstly, as the OT camera monitors the spatter through long exposure, the quality of the monitored data is not affected by the temporal resolution of the camera. Secondly, only the spatter particles that land on the powder bed but not consumed by the laser melting process are considered for degradation of powder feedstock. Spatter particles that redeposit on part surface or melted by the laser beam later on influence the part quality as illustrated by [34,37,38], but are not to be concerned for the quality control of reused feedstock powder. It is therefore appropriate to conduct the analysis layer-by-layer instead of track-by-track considering the scope and purpose of the study. Thirdly, the OT system only detects incandescent particles that emit light due to their high temperature, cold ejecta that do not encounter the laser beam are not included in the analysis. It is assumed that the ejecta exhibiting incandescence contribute to the majority of powder oxidation. Finally, the segmentation of the collected images is based on the

geometry of the part using the STL design files as the guidance to separate the pixels for laser-irradiated area and spatter regions, which does not involve image thresholding techniques used in [34–36].

4.2. Correlation between the OT data and powder oxidation

A distinction can be made between the more degraded powder samples from the L3D1 and L7D3 containers and the less degraded powder samples from the empty and L7D1 containers based on the bulk oxygen content (Fig. 7). Although the oxygen content results in Fig. 7 suggest the L7D3 power is the most oxidized one, the total sum of GVs in spatter region, ΣS_s (Fig. 12a) shows that more spatter is observed in the L3D1 sample. One needs to consider the sampling process during the experiment to explain this discrepancy. Since the four containers possess different volumes of cavities inside (V_c), the spatter particles ejected during the L-PBF process were mixed with different volumes of feedstock powder that was in virgin state for the current study. The mixing of spatter and the virgin powder dilutes the amount of oxygen to different extents for the four container samples. To make correlation between the OT data and the measured oxygen content in Fig. 7, the total sum of GVs in the spatter region, ΣS_s , must be normalized by the volume of cavity, V_c . Thus, the quantity $\Sigma S_s/V_c$ can be related to the concentration of spatter particles in the collected powder samples. The order in which the four containers rank in $\Sigma S_s/V_c$ according to Fig. 12b (L7D3 > L3D1 > L7D1 > Empty) agrees with the ranking of oxygen uptake values in Fig. 12c. Future works strategically varying lattice structures inside the powder containers to produce more data for Analysis of Variance (ANOVA) is needed to further confirm this correlation. Here the oxygen uptake is calculated as the difference between virgin powder and the powder samples from the four containers in bulk oxygen contents shown in Fig. 7. It is necessary to clarify that the oxygen level in the process chamber can have significant impact on the oxidation of the spatter and the correlation found in this study is only applicable to the condition where a 1000 ppm oxygen level control is applied. As reported by Raza et al. [9], stricter control of the oxygen level in the process chamber under 20 ppm can mitigate the surface oxidation of the IN718 powder but would not prevent spattering. It is recommended for future work to apply the proposed methodology in this paper to investigate the influence of oxygen level in the build chamber on spattering and powder degradation.

4.3. Influence of part geometry on powder degradation

The current study has identified two geometrical factors for the introduction of spatter into the powder bed and the consequent degradation of powder to be reused, namely large volume of overhangs and large surface areas of the parts.

Firstly, lattices of different beam width and length (Fig. 1) are essentially overhanging structures with varied height and cross-sectional areas. Although the current study does not deal with the mechanisms of spatter formation, it is suspected that the overhang features exacerbate spattering by one of the two following mechanisms or a combination of both. On one hand, since the powder surrounding the melt pools has higher absorptivity [39] and has lower thermoconductivity [40] compared to its bulk metal counterpart, the heat input by the laser is locally intensified and accumulated at overhanging structures. This overheating effect (intensification and accumulation of laser heat) is captured by the OT images as the L7D3 container shows higher GVs in the laser-irradiated region of OT images (e.g., Fig. 4a Z = 24.88 mm) where the lattice beams diverge from vertexes. Analogous to previous findings where higher laser energy input leads to more spattering [34,37], the overheating at overhangs can also lead to more intensive spattering (e.g., Fig. 4b Z = 24.88 mm). This overheating phenomenon is not found in the L7D1 and L3D1 containers, as the lattices of smaller beam diameter show lower GVs in the laser-irradiated regions of OT images (Fig. 5e). On the other hand, the large overhang

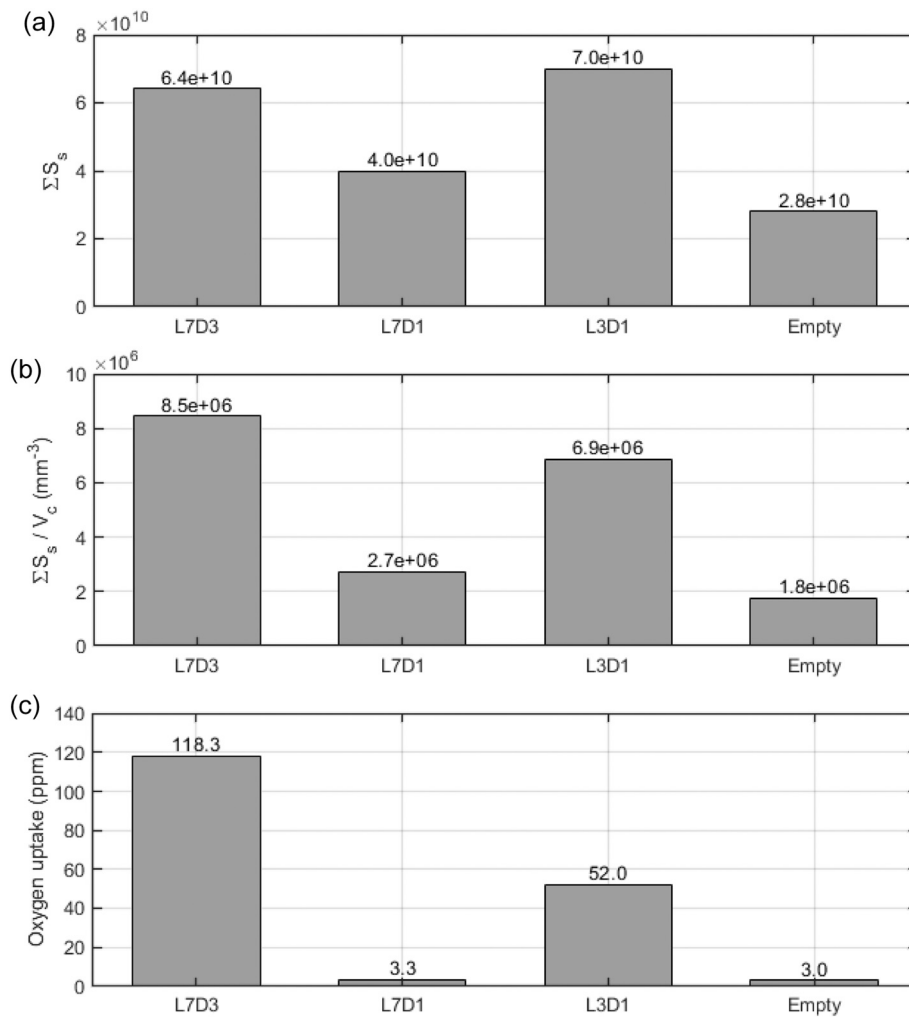


Fig. 12. Comparisons of (a) total GV in the spatter region ΣS_s , (b) GV per unit volume of cavity in the container $\Sigma S_b/V_c$, (c) oxygen uptake compared to virgin state in the four containers.

areas are supported by free-to-move powder particles during the laser-powder interactions, which can lead to more particles entrained by the vapor plume and oxidized [16] [18].

Secondly, a part with larger surface area provides more interfaces between the part and surrounding powder, allowing more spatter particles to be introduced to the powder bed. Meanwhile, the volume of the part dictates the amount of powder processed by the laser and hence the amount of spatter generated. The question is raised as to what proportion the spatter particles generated are introduced to the powder bed to affect the quality of the powder for reuse rather than getting re-melted by the laser. One can approach the problem by examining the correlation between the surface area of the part and the observed GV in the spatter region of OT images. The perimeter (P_l) and area (A_l) of the laser-irradiated region are equivalent to the surface area and volume of the 3D part respectively. The ratio P_l/A_l is plotted in Fig. 13a for each layer in the four containers. The sum of GV in the spatter region normalized by area of laser exposure for each layer S_s/A_l , is plotted in Fig. 13b. While the curves in Fig. 13a and b show different local oscillations and overlaps, in general when normalized by the area of laser exposure (A_l), the container geometry with larger perimeter in 2D layers has higher sum of GV in the spatter region. The same comparison holds in 3D as the surface area of the part and the total sum of GV in the spatter region (summation over all layers), ΣS_s , are normalized by the volume of the part (shown in Fig. 13b and d). According to Fig. 13, it is reasonable to hypothesize that with fixed volume of material processed by the L-PBF

process, parts or builds with higher surface-to-volume ratios would introduce more spatter to the powder that surrounds the parts.

5. Conclusions

In this work, data are extracted from the optical tomography images for analysis of spattering, showing correlations between the OT data, the powder degradation and part geometry. Components of higher surface-to-volume ratio (L3D1) and larger areas of overhangs (L7D3) are found to generate more spatter during the L-PBF process. The oxygen content increased by ~118 ppm (49 % relative to virgin state) in the case of L7D3, followed by an increase of 52 ppm (22 % relative to virgin state) in the case of L3D1. XPS surface analyses of the powder show extensive powder surface oxidation by the formation of Al-rich and Cr-rich oxides. With a given volume of material built, a higher surface-to-volume ratio allows more process by-products to be introduced to the reused powder rather than being re-melted by the laser during the building process. The overhanging structures incur local overheating and, in the meantime, produces more spatter particles and affect the quality of the cycled powder upon the finish of a L-PBF build job. Based on the findings of the current study, large surface-to-volume ratio and large areas of overhangs are identified as critical geometrical factors for powder degradation. It is therefore recommended to evaluate these factors when it comes to the comparison of powder batches of similar number of cycles or to integrate such geometrical quantities into the powder usage history. Moreover,

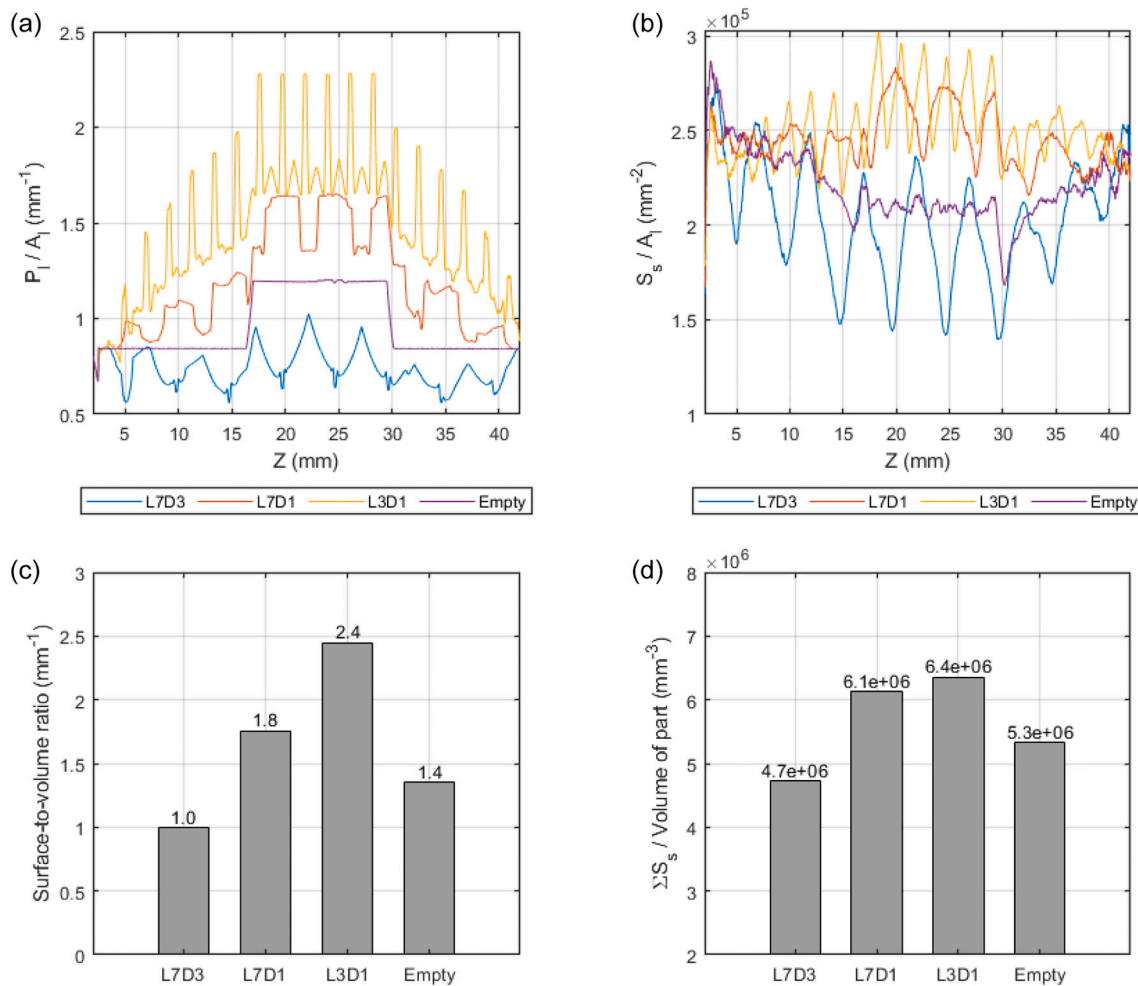


Fig. 13. Line plots show (a) perimeter to area ratio of the laser-irradiated region and (b) Sum of GVs in spatter regions normalized by the area of the laser-irradiated region, S_s/A_l , along the build height direction. Here P_l and A_l denote the perimeter and area of the laser-irradiated region in a layer. Bar graphs show (c) surface-to-volume ratio determined from the CAD files of the four containers and (d) sum of in GVs in spatter region for all layers normalized by the volume of part (amount of material processed by the laser) in the four containers.

the powder container designs presented in this work have implications for powder sampling for different purposes. For a given combination of processing conditions (machine, gas purity, laser processing parameters) and powder (alloy type, grade), using a container sample of high surface-to-volume ratio, like L3D1, allows rapid and robust evaluations of powder degradation. On the other hand, a container design like the empty container can be used to capture powder as witness samples for the state of the powder feedstock used in a build job. For future works, it is of interest to conduct systematic research on powder degradation over many builds while keeping record of part geometry and applying the OT image analysis. The outcome of such research would lead to more confidence in the prediction of powder reusability over long term.

Declaration of competing interest

The authors declare that they have no known competing financial interests or personal relationships that could have appeared to influence the work reported in this paper.

Acknowledgement

This work has been conducted in the framework of the Centre for Additive Manufacture–Metal (CAM²) supported by the Swedish Governmental Agency for Innovation Systems (Vinnova). Funding from the European Union's Horizon 2020 research and Innovation

Programme Additive Manufacturing using Metal Pilot Line (MANUELA) under grant agreement n°820774 is gratefully acknowledged. Experimental assistance from Mr. Anton Dahl-Jendelin is greatly appreciated.

Appendix A. Supplementary data

Supplementary data to this article can be found online at <https://doi.org/10.1016/j.jmapro.2022.07.031>.

References

- [1] Frazier WE. In: Metal additive manufacturing: a review. 23; 2014. p. 1917–28. <https://doi.org/10.1007/s11665-014-0958-z>.
- [2] Chua CK, Wong CH, Yeong WY. Quality management framework in additive manufacturing. In: Stand qual control meas sci 3D print addit manuf; 2017. p. 213–39. <https://doi.org/10.1016/b978-0-12-813489-4.00009-x>.
- [3] Slotwinski JA, Garboczi EJ, Stutzman PE, Ferraris CF, Watson SS, Peltz MA. Characterization of metal powders used for additive manufacturing. J Res Natl Inst Stand Technol 2014;119:460–93. <https://doi.org/10.6028/jres.119.018>.
- [4] Cordova L, Campos M, Tinga T. Revealing the effects of powder reuse for selective laser melting by powder characterization. JOM 2019;71:1062–72. <https://doi.org/10.1007/s11837-018-3305-2>.
- [5] Gasper AND, Szost B, Wang X, Johns D, Sharma S, Clare AT, et al. Spatter and oxide formation in laser powder bed fusion of inconel 718. Addit Manuf 2018;24:446–56. <https://doi.org/10.1016/j.addma.2018.09.032>.
- [6] Snow Z, Martukanitz R, Joshi S. On the development of powder spreadability metrics and feedstock requirements for powder bed fusion additive manufacturing. Addit Manuf 2019;28:78–86. <https://doi.org/10.1016/j.addma.2019.04.017>.

- [7] Tan JH, Wong WLE, Dalgarno KW. An overview of powder granulometry on feedstock and part performance in the selective laser melting process. *Addit Manuf* 2017;18:228–55. <https://doi.org/10.1016/j.addma.2017.10.011>.
- [8] Pauzon C, Raza A, Hryha E, Forêt P. Oxygen balance during laser powder bed fusion of alloy 718. *Mater Des* 2021;201:109511. <https://doi.org/10.1016/j.matdes.2021.109511>.
- [9] Raza A, Pauzon C, Hryha E, Markström A, Forêt P. Spatter oxidation during laser powder bed fusion of alloy 718: dependence on oxygen content in the process atmosphere. *Addit Manuf* 2021;48. <https://doi.org/10.1016/j.addma.2021.102369>.
- [10] Neiva E, Chiumenti M, Cervera M, Salsi E, Piscopo G, Badia S, et al. Numerical modelling of heat transfer and experimental validation in powder-bed fusion with the virtual domain approximation. *Finite Elem Anal Des* 2020;168:103343. <https://doi.org/10.1016/j.finel.2019.103343>.
- [11] Hryha E, Shvab R, Gruber H, Leicht A, Nyborg L. Surface oxide state on metal powder and its changes during additive manufacturing: an overview. In: *Proc euro PM 2017 int powder metall Congr exhib*; 2018.
- [12] Khairallah SA, Anderson AT, Rubenchik AM, King WE. Laser powder-bed fusion additive manufacturing: physics of complex melt flow and formation mechanisms of pores, spatter, and denudation zones. *Acta Mater* 2016;108:36–45. <https://doi.org/10.1016/j.actamat.2016.02.014>.
- [13] Bidare P, Bitharas I, Ward RM, Attallah MM, Moore AJ. Fluid and particle dynamics in laser powder bed fusion. *Acta Mater* 2018;142:107–20. <https://doi.org/10.1016/j.actamat.2017.09.051>.
- [14] Simonelli M, Tuck C, Aboulkhair NT, Maskery I, Ashcroft I, Wildman RD, et al. A study on the laser spatter and the oxidation reactions during selective laser melting of 316L stainless steel, Al-Si10-mg, and ti-6Al-4V. *Metall Mater Trans A Phys Metall Mater Sci* 2015;46:3842–51. <https://doi.org/10.1007/s11661-015-2882-8>.
- [15] Young ZA, Guo Q, Parab ND, Zhao C, Qu M, Escano LI, et al. Types of spatter and their features and formation mechanisms in laser powder bed fusion additive manufacturing process. *Addit Manuf* 2020;36:101438. <https://doi.org/10.1016/j.addma.2020.101438>.
- [16] Matthews MJ, Guss G, Khairallah SA, Rubenchik AM, Depond PJ, King WE. Denudation of metal powder layers in laser powder bed fusion processes. *Acta Mater* 2016;114:33–42. <https://doi.org/10.1016/j.actamat.2016.05.017>.
- [17] Nassar AR, Gundermann MA, Reutzel EW, Guerrier P, Krane MH, Weldon MJ. Formation processes for large ejecta and interactions with melt pool formation in powder bed fusion additive manufacturing. *Sci Rep* 2019;9. <https://doi.org/10.1038/s41598-019-41415-7>.
- [18] Ly S, Rubenchik AM, Khairallah SA, Guss G, Matthews MJ. Metal vapor micro-jet controls material redistribution in laser powder bed fusion additive manufacturing. *Sci Rep* 2017;7:1–12. <https://doi.org/10.1038/s41598-017-04237-z>.
- [19] Gorji NE, Saxena P, Corfield M, Clare A, Rueff J-P, Bogan J, et al. A new method for assessing the recyclability of powders within powder bed fusion process. *Mater Charact* 2020;161:110167. <https://doi.org/10.1016/j.matchar.2020.110167>.
- [20] Moghimi P, Poiré T, Habibnejad-Korayem M, Zavala JA, Kroeger J, Marion F. Metal powders in additive manufacturing: a review on reusability and recyclability of common titanium, nickel and aluminum alloys. *Addit Manuf* 2021;43:102017. <https://doi.org/10.1016/j.addma.2021.102017>.
- [21] Ladewig A, Schlick G, Fisser M, Schulze V, Glatzel U. Influence of the shielding gas flow on the removal of process by-products in the selective laser melting process. *Addit Manuf* 2016;10:1–9. <https://doi.org/10.1016/j.addma.2016.01.004>.
- [22] Wang XJ, Zhang LC, Fang MH, Sercombe TB. The effect of atmosphere on the structure and properties of a selective laser melted Al-12Si alloy. *Mater Sci Eng A* 2014;597:370–5. <https://doi.org/10.1016/j.msea.2014.01.012>.
- [23] Pauzon C, Leicht A, Klement U, Forêt P, Hryha E. Effect of the process gas and scan speed on the properties and productivity of thin 316L structures produced by laser-powder bed fusion. *Metall Mater Trans A Phys Metall Mater Sci* 2020;51. <https://doi.org/10.1007/s11661-020-05923-w>.
- [24] Shen H, Rometsch P, Wu X, Huang A. Influence of gas flow speed on laser plume attenuation and powder bed particle pickup in laser powder bed fusion. *JOM* 2020;72:1039–51. <https://doi.org/10.1007/s11837-020-04020-y>.
- [25] Philo AM, Sutcliffe CJ, Sillars S, Sienz J, Brown SGR, Lavery NP. A study into the effects of gas flow inlet design of the Renishaw AM250 laser powder bed fusion machine using computational modelling. In: *Solid free fab 2017 proc 28th annu int solid free fab sym - an addit manuf conf SFF* 2017; 2020. p. 1203–19.
- [26] Ferrar B, Mullen L, Jones E, Stamp R, Sutcliffe CJ. Gas flow effects on selective laser melting (SLM) manufacturing performance. *J Mater Process Technol* 2012;212:355–64. <https://doi.org/10.1016/j.jmatprotec.2011.09.020>.
- [27] Schniedenharn M, Wiedemann F, Schleifenbaum JH. Visualization of the shielding gas flow in SLM machines by space-resolved thermal anemometry. *Rapid Prototyp J* 2018;24:1296–304. <https://doi.org/10.1108/RPJ-07-2017-0149>.
- [28] Zenzinger G, Bamberg J, Ladewig A, Hess T, Henkel B, Satzger W. Process monitoring of additive manufacturing by using optical tomography. *AIP Conf Proc* 2015;1650:164–70. <https://doi.org/10.1063/1.4914606>.
- [29] Adam A. Mesh voxelisation. MATLAB Cent File Exch. <https://www.mathworks.com/matlabcentral/fileexchange/27390-mesh-voxelisation>. [Accessed 5 July 2021].
- [30] Patil S, Ravi B. Voxel-based representation, display and thickness analysis of intricate shapes. In: *Proc - ninth int conf comput aided des comput graph CAD/CG* 2005. 2005; 2005. p. 415–20. <https://doi.org/10.1109/CAD-CG.2005.86>.
- [31] Whiting JG, Garboczi EJ, Tondare VN, Scott JHH, Donmez MA, Moylan SP. A comparison of particle size distribution and morphology data acquired using lab-based and commercially available techniques: application to stainless steel powder. *Powder Technol* 2022;396:648–62. <https://doi.org/10.1016/j.powtec.2021.10.063>.
- [32] Whiting J, Fox J. Characterization of feedstock in the powder bed fusion process: sources of variation in particle size distribution and the factors that influence them. In: *Solid free fab 2016 proc 27th annu int solid free fab sym - an addit manuf conf SFF* 2016; 2016. p. 1057–68.
- [33] Gruber H, Henriksson M, Hryha E, Nyborg L. Effect of powder recycling in electron beam melting on the surface chemistry of alloy 718 powder. *Metall Mater Trans A Phys Metall Mater Sci* 2019;50:4410–22. <https://doi.org/10.1007/s11661-019-05333-7>.
- [34] Repossini G, Laguzza V, Grasso M, Colosimo BM. On the use of spatter signature for in-situ monitoring of laser powder bed fusion. *Addit Manuf* 2017;16:35–48. <https://doi.org/10.1016/j.addma.2017.05.004>.
- [35] Taheri Andani M, Dehghani R, Karamooz-Ravari MR, Mirzaeifar R, Ni J. Spatter formation in selective laser melting process using multi-laser technology. *Mater Des* 2017;131:460–9. <https://doi.org/10.1016/j.matdes.2017.06.040>.
- [36] Barrett C, Carradero C, Harris E, Rogers K, MacDonald E, Conner B. Statistical analysis of spatter velocity with high-speed stereovision in laser powder bed fusion. *Prog Addit Manuf* 2019;4:423–30. <https://doi.org/10.1007/s40964-019-00094-6>.
- [37] Taheri Andani M, Dehghani R, Karamooz-Ravari MR, Mirzaeifar R, Ni J. A study on the effect of energy input on spatter particles creation during selective laser melting process. *Addit Manuf* 2018;20:33–43. <https://doi.org/10.1016/j.addma.2017.12.009>.
- [38] Ciales LE, Arisoy YM, Lane B, Moylan S, Donmez A, Özel T. Laser powder bed fusion of nickel alloy 625: experimental investigations of effects of process parameters on melt pool size and shape with spatter analysis. *Int J Mach Tool Manuf* 2017;121:22–36. <https://doi.org/10.1016/j.ijmachtools.2017.03.004>.
- [39] Trapp J, Rubenchik AM, Guss G, Matthews MJ. In situ absorptivity measurements of metallic powders during laser powder-bed fusion additive manufacturing. *Appl Mater Today* 2017;9:341–9. <https://doi.org/10.1016/j.apmt.2017.08.006>.
- [40] Zhang S, Lane B, Whiting J, Chou K. On thermal properties of metallic powder in laser powder bed fusion additive manufacturing. *J Manuf Process* 2019;47:382–92. <https://doi.org/10.1016/j.jmapro.2019.09.012>.